Quaternary Science Reviews 225 (2019) 105981

Contents lists available at ScienceDirect

Quaternary Science Reviews

journal homepage: www.elsevier.com/locate/quascirev

New *in situ* ^{14}C data indicate the absence of nunataks in west Greenland during the Last Glacial Maximum

Brandon L. Graham [a, *], Jason P. Briner [a], Avriel D. Schweinsberg [a], Nathaniel A. Lifton [b, c], Ole Bennike [d]

[a] *Department of Geology, University at Buffalo, Buffalo, NY 14260, USA*
[b] *Department of Earth, Atmospheric, and Planetary Sciences, Purdue University, West Lafayette, IN 47907, USA*
[c] *Department of Physics and Astronomy, Purdue University, West Lafayette, IN 47907, USA*
[d] *Geological Survey of Denmark and Greenland, Øster Voldgade 10, DK-1350 Copenhagen k, Denmark*

A R T I C L E I N F O

Article history:
Received 11 June 2019
Received in revised form
25 September 2019
Accepted 3 October 2019
Available online xxx

Keywords:
Holocene
Pleistocene
Greenland
Cosmogenic *in situ* ^{14}C
Neoglaciation
Modelling

A B S T R A C T

In situ cosmogenic nuclide exposure age distributions on Ice Age nunataks act as past ice thickness indicators and provide valuable targets for ice sheet model simulations of the Last Glacial Maximum. Several locations along West Greenland have been identified as being potential nunataks due to their weathered nature and their high cosmogenic nuclide inventories with little evidence for ice sheet burial. We present new *in situ* cosmogenic ^{14}C measurements from four high elevation surfaces in the central Uummannaq Fjord system that were identified as potential nunataks in prior work. Building on previous work, we model cosmogenic radionuclide production and decay, and consider a range of ice sheet history scenarios. Since our results require more burial or shielding under ice than what independent methods suggest for Holocene ice cap cover, we propose that these locations were not nunataks during the Last Glacial Maximum, but rather were buried during the peak of the Last Glacial Maximum. However, we cannot confirm whether these sites were buried by the Greenland Ice Sheet or local glaciers.

1. Introduction

Empirical data of ice sheet size during Quaternary glaciations provide important constraints for ice sheet modelling, sea level budgets, glacio-isostatic adjustment calculations and climate sensitivity. Although our understanding of Greenland Ice Sheet (GrIS) size during the Last Glacial Maximum (LGM; 26–19 ka) is improving (Funder et al., 2011; Lecavalier et al., 2014; Vasskog et al., 2015), both the lateral extent and thickness of the GrIS during the LGM remain uncertain. Because the GrIS terminated on the continental shelf during the LGM, the position of the LGM terminus is somewhat obscured and requires detailed studies offshore (O'Cofaigh et al., 2013; Arndt et al., 2017). This work is ongoing and has resulted in recent refinements of the LGM ice extent.

In terms of the thickness of the GrIS, prior work has suggested that distal high-elevation summits in coastal western Greenland may have been nunataks during the LGM. If such nunataks can be confirmed, they would provide important constraints for ice sheet models. Kelly (1985) described uplands in southwestern Greenland that exhibit highly weathered bedrock and a lack of features associated with glacial erosion, indicating possible ice-free areas at high elevation. Rinterknecht et al. (2009) were the first to obtain cosmogenic nuclide exposure ages (^{10}Be only) from some of these regions and found nuclide concentrations in both boulders and bedrock samples that were too high to be explained by post-LGM exposure. The pattern of cosmogenic nuclide concentration versus elevation was described more fully by Roberts et al. (2009), who suggested the presence of LGM nunataks as well as confluent inland and local ice near Sisimiut in western Greenland. Challenging these conclusions are studies from elsewhere in polar regions demonstrating that cold-based portions of ice sheets may cover, but not erode, upland surfaces (e.g., Bierman et al., 1999; Briner et al., 2003, 2006), leading to significant cosmogenic nuclide inheritance.

Roberts et al. (2013) and Lane et al. (2014) measured cosmogenic nuclide concentrations in bedrock samples from high-elevation areas bordering the deep marine troughs in the Uummannaq Fjord system (Fig. 1). They combined ^{10}Be and ^{26}Al measurements

* Corresponding author. 126 Cooke Hall, University at Buffalo, Buffalo, NY 14260, USA.
E-mail address: blgraham@buffalo.edu (B.L. Graham).

https://doi.org/10.1016/j.quascirev.2019.105981
0277-3791/

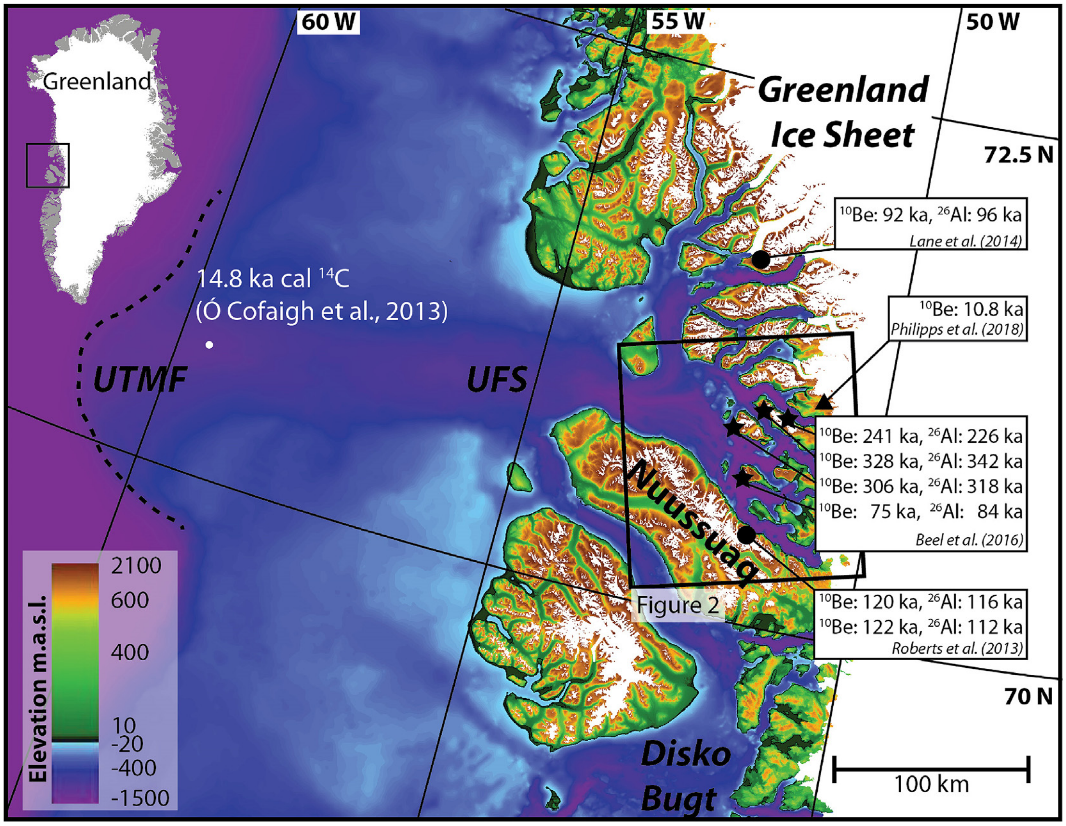

Fig. 1. The Uummannaq Fjord System (UFS). The white circle is a calibrated radiocarbon age above till, providing a minimum age for the onset of deglaciation from the shelf edge. The black circles are relevant cosmogenic nuclide data from previous published studies. The black triangle is the age when the GrIS retreated behind the historical margin. The black stars are the sample locations of this study. UTMF = Uummannaq Trough Mouth Fan. Elevation and Bathymetry shown with a non-linear color bar to highlight features such as the fjord troughs and high elevations. Background image from BedMachine V3 (Morlighem et al., 2017). (For interpretation of the references to color in this figure legend, the reader is referred to the Web version of this article.)

and noted high concentrations of both nuclides, and generally concordant isotopic relationships that results from continuous exposure without significant (~90 kyr or more) cumulative ice sheet burial at their sample locations. The concordant relationship was readily observed by the consistent ^{26}Al/^{10}Be canonical production ratio of ~6.75:1 (7.3 ± 0.3, (Corbett et al., 2017)). Corbett et al. (2013) measured paired ^{10}Be and ^{26}Al in a number of high-elevation samples farther north, near Upernavik. It was found that discordant isotopic relationships resulting from the observable radioactive decay of ^{26}Al suggested that significant durations (>90 kyr) of cold-based ice cover have occurred at high elevations in the Upernavik region of west-central Greenland. A limitation of these approaches, however, is that ^{26}Al and ^{10}Be data alone cannot be used to constrain when the burial may have occurred, for example, during a specific glacial episode such as the LGM. In addition, due to the long half-lives (^{10}Be $t_{1/2}$ = 1390 kyr; ^{26}Al $t_{1/2}$ = 705 kyr), and measurement uncertainties, significant durations of shielding or burial under ice is required to definitively observe a discordant relationship.

In most regions around the Arctic, paired ^{10}Be and ^{26}Al measurements show evidence of ice sheet burial in the form of isotopic discordance (Gjermundsen et al., 2015). Due to the unique findings of Roberts et al. (2013) and Lane et al. (2014) that some surfaces record long exposure durations (~100 kyr) but lack isotope discordance, Beel et al. (2016) visited several new high-elevation sites in the central Uummannaq Fjord system. They measured four samples with surprisingly high concentrations of ^{10}Be and ^{26}Al (equivalent up to ~330 kyr of exposure) with no detectable isotopic discordance. This led Beel et al. (2016) to postulate that some uplands in the central Uummannaq Fjord system may have been nunataks during the LGM despite being >300 km inland of the LGM terminus at the continental shelf break (Fig. 1; O'Cofaigh et al., 2013).

Here, we report new *in situ* cosmogenic ^{14}C (*in situ* ^{14}C) data from the four bedrock samples that contain the highest ^{10}Be and ^{26}Al concentrations measured by Beel et al. (2016). Given the short half-life of *in situ* ^{14}C (5700 yr), it is much more sensitive to short-lived and recent burial than ^{10}Be and ^{26}Al, such as during the LGM (Hippe, 2017; Young et al., 2018; Briner et al., 2014). Thus, *in situ* ^{14}C measurements should constrain whether uplands bordering the Uummannaq Fjord system were nunataks during the LGM. Complicating our experiment is the fact that the four sample locations were all collected from within a few meters of receding local ice cap margins, indicating that all experienced burial during portions of the Holocene (Fig. 2; Schweinsberg et al., 2017). To determine the duration of Holocene ice cap burial, and to factor burial into our calculations of LGM history, we use radiocarbon ages obtained from *in situ* tundra moss adjacent to each rock sample (Schweinsberg et al., 2017). Once exposed by ice margin retreat, these mosses in growth position are rapidly removed by water or wind erosion in a few years, or begin to regrow and reset the radiocarbon clock with modern atmospheric concentrations (Miller et al., 2013). We thus estimate that the rock samples became fully exposed from their Late Holocene ice-cover within a year or two of their collection in 2013 (Walker et al., 2018). These radiocarbon ages provide the time that ice cap growth most recently covered the

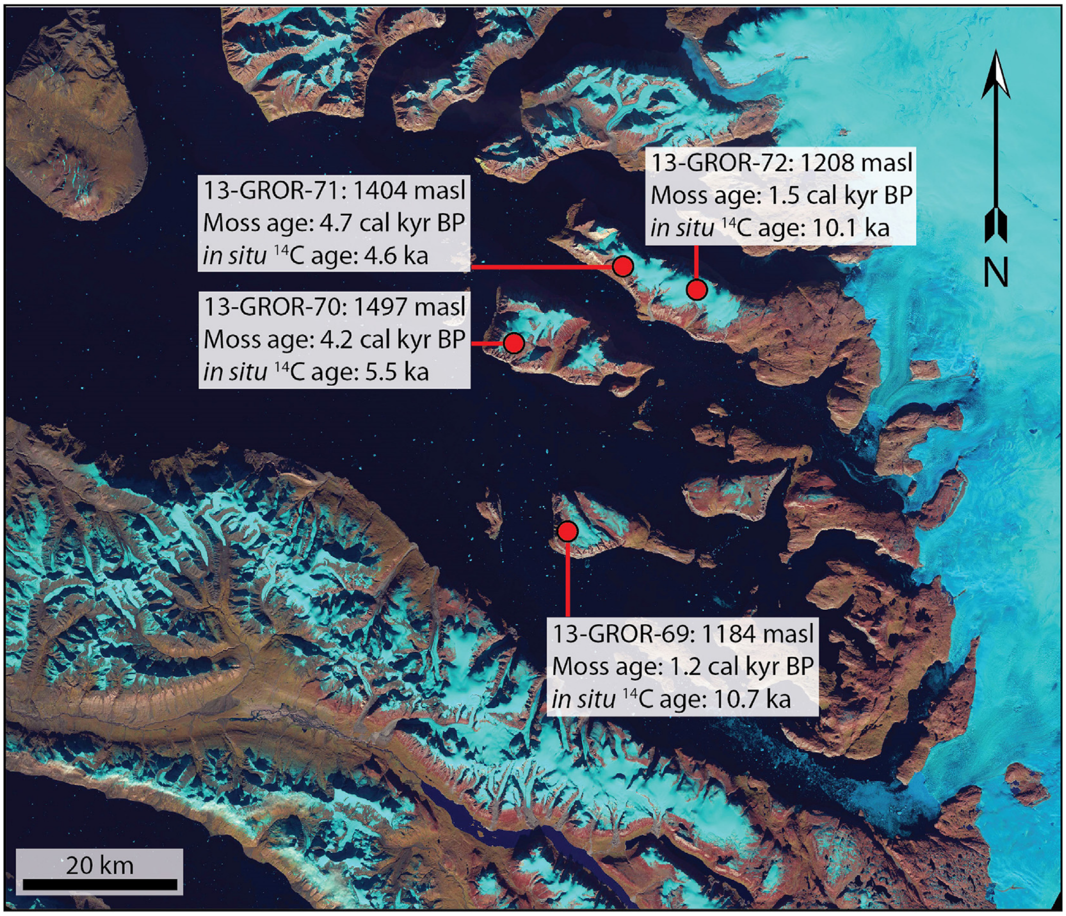

Fig. 2. Sample locations in this study (red circles). Moss ages from Schweinsberg et al. (2017). Cosmogenic *in situ* ^{14}C ages are apparent ages only. Base image is a Landsat 8 scene acquired on September 21, 2018. (For interpretation of the references to color in this figure legend, the reader is referred to the Web version of this article.)

sampled bedrock surfaces during the latter stages of the Holocene by entombing and preserving the mosses (Anderson et al., 2008; Miller et al., 2013; Schweinsberg et al., 2017), a climate trend well described in Greenland (Briner et al., 2016; McKay et al., 2018). When accounting for periods of Holocene shielding by local ice caps, we find that the *in situ* ^{14}C concentrations are too low to be consistent with continuous exposure throughout the LGM, and thus find it likely that the central Uummannaq fjord uplands experienced ice cover during the LGM.

2. Methods and approach

Quartz-bearing rock samples were collected from the Uummannaq region in 2013 for ^{10}Be, ^{26}Al, and ^{14}C measurement (Fig. 3). High-elevation weathered blockfield (felsenmeer) slabs were sampled at the front of the present day retreating local ice caps. Large rock slabs were sampled; these may still be rooted into intact bedrock. In addition, *in situ* dead vegetation (moss) was sampled (Beel et al., 2016; Schweinsberg et al., 2017). Rock sample sites were chosen partly based on the presence of weathering pits, indicating long-term stability and existence at the surface, minimal glacial erosion, and an increased likelihood of the surfaces being securely in place through multiple glacial-interglacial cycles. We collected samples with a hammer and chisel away from edges and corners. We recorded latitude, longitude, elevation, surface dip and dip direction, and topographic shielding measurements. The four samples analyzed here range in elevation from 1184 to 1497 m above sea level (asl), as collected by a handheld GPS with an uncertainty of ±10 m.

Samples were physically and chemically processed at the Purdue Rare Isotope Measurement Laboratory (PRIME Lab) at Purdue University, U.S.A. *In situ* ^{14}C was extracted from purified quartz separates for each sample through automated procedures (Lifton et al., 2015). Approximately 5–10 g of quartz from each sample was added to a degassed $LiBO_2$ flux in an Al_2O_3 sample boat and heated to 600 °C for 1 h in ca. 50 torr of Research Purity O_2 to remove atmospheric contaminants, which were discarded. The sample was then heated to 1100 °C for 3 h to dissolve the quartz and release the *in situ* ^{14}C; this was also completed in an atmosphere of 50 torr of Research Purity O_2 to oxidize any evolved carbon species to CO_2. The CO_2 from the 1100 °C step was then purified, measured quantitatively, and converted to graphite for ^{14}C AMS measurement at PRIME Lab (Lifton et al., 2015). Measured concentrations of *in situ* ^{14}C are calculated from the measured isotope ratios via accelerator mass spectrometry following Hippe and Lifton (2014).

As mentioned above, previous work analyzed the relationship between ^{10}Be and ^{26}Al concentrations (Beel et al., 2016). Our study focuses on forward modelling of exposure and burial scenarios required to identify complex exposure scenarios consistent with both the moss radiocarbon ages and the measured *in situ* ^{14}C concentration. Due to its short half-life, *in situ* ^{14}C reaches a secular equilibrium between production and decay (saturation) within ca. 30 kyr (Fig. 4 at 100 ka), and decays to current detection limits in ca. 30 kyr of complete burial (Fig. 4 at 40 ka) (Miller et al., 2006; Hippe,

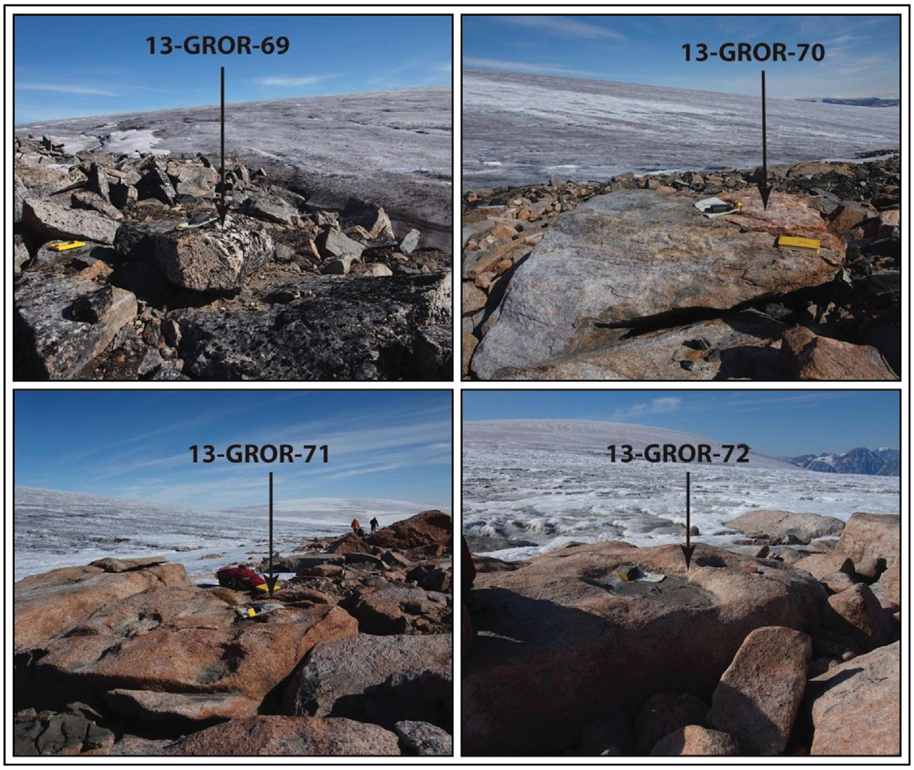

Fig. 3. Field locations for samples collected in this study. All samples were collected from autochthonous blockfield slabs that exhibited weathering pits and weathered surfaces. Note the close proximity to the local ice cap margin.

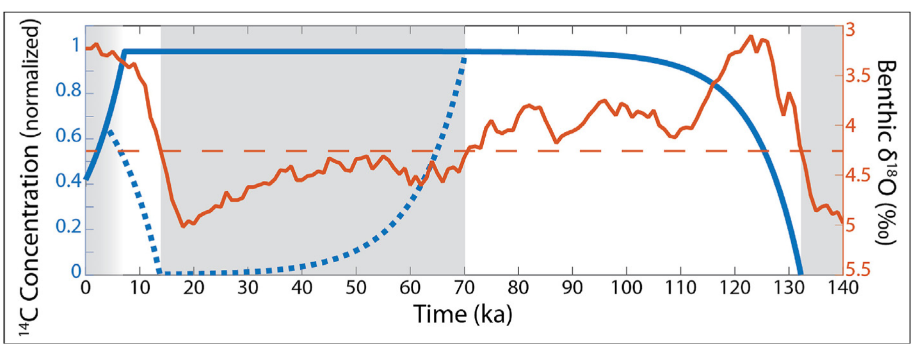

Fig. 4. Hypothetical *in situ* ^{14}C concentrations (normalized, 1 = saturation) through time showing continuous exposure (nunatak: blue solid line) and Marine Isotope Stage (MIS) 4-2 burial required for complete nuclide decay (ice cover: blue dotted line). This model assumes complete isotopic decay during the MIS 6 glaciation and begins exposure at the onset of MIS 5e (~130 ka) once global ice volume decreases (orange threshold). Note how after ~30 kyr of burial (at 40ka), the concentration decays away to background detectable limits. Grey bars represent periods of glacial burial. The solid orange line is the benthic δ^{18}O stack from Lisiecki and Raymo (2005) and the dashed orange line is the glacial threshold value. (For interpretation of the references to color in this figure legend, the reader is referred to the Web version of this article.)

2017; Young et al., 2018). Thus, *in situ* ^{14}C measurements are insensitive to burial/exposure events occurring before 30–40 ka (Fig. 4).

Exposure-burial scenarios were modelled in Matlab r2018a. Each sample is modelled using a site-specific, time dependent *in situ* ^{14}C production rate (Phillips et al., 2016; Borchers et al., 2016; Balco, 2017) using the LSD*n* scaling framework (Lifton et al., 2014). Development of Holocene ice caps over our sample locations requires that a complex Holocene exposure/burial history occurred. Significant long-term burial of the sample locations is not supported by the high ^{10}Be and ^{26}Al concentrations, each of which consistent with continuous exposure (Beel et al., 2016). Constrained by the radiocarbon ages from the ice-killed surface moss, which provides the timing of burial by ice cap growth during the Holocene, equation (1) is solved for burial (glacial onset) and exposure (glacial retreat) ages in 10-year increments from the associated moss age to 70 ka and from the associated moss age to 30 ka, respectively:

where N_p is the predicted/modelled concentration (at g^{-1}), P is the cumulative muon and spallation production rate (atoms g^{-1} yr^{-1}), λ is the decay constant for ^{14}C (yr^{-1}), $t_{e.1\text{-}2}$ are the two durations of exposure, and $t_{b.1\text{-}2}$ are the two durations of burial (yr), with $t_{b.2}$ set as the moss age.

$$N_p = P/_{\lambda}(1-\exp(-\lambda t_{e.1}))\exp(-\lambda(t_{b.1}+t_{e.2}+t_{b.2})) + P/_{\lambda}(1-\exp(-\lambda t_{e.2}))\exp(-\lambda t_{b.2}) \quad (1)$$

The initial exposure, $t_{e.1}$, begins at 130 ka (the transition from Marine Isotope Stage (MIS) 6 to MIS 5e) with no initial *in situ* ^{14}C concentration. All combinations for burial and exposure are computed to solve for the final nuclide concentration. To constrain the possible ranges of $t_{b.1}$ and $t_{e.2}$, a maximum age of burial is set to 70 ka and a maximum age of re-exposure is set to 30 ka due to the insensitivity of *in situ* ^{14}C to older ages, respectively. The predicted concentration, N_p, is compared to the measured concentration, N_m, and normalized to the associated analytical 1 sigma uncertainty, σ, through the z-score, z:

$$z = \frac{|N_p - N_m|}{\sigma} \quad (2)$$

The simple model finds the z-score for every burial/exposure scenario, in 10-year increments, for each of the four samples to create a burial/exposure curve of plausible solutions with 1, 2, and 3 sigma analytical uncertainty. These contour plots are utilized for determining plausible burial/exposure scenarios through time for each sample (Fig. 5).

For this analytical solution to be used, several assumptions are made. Due to the antiquity of surfaces in felsenmeer terrain, it is assumed that no measurable glacial erosion or subaerial erosion has occurred in the past 130 kyr at our sample sites. To test this assumption, a sensitivity test was performed to determine the subaerial constant erosion rate required for these sites to be nunataks. It was determined that a rate of 0.4 mm yr^{-1} is needed, or an equivalent of 40 m of bedrock be removed in 100 kyr − an implausible scenario given the field evidence for surface stability. Similarly, the development of weathering pits in more temperate environments has been shown to occur several orders of magnitude more slowly (Hall and Phillips, 2006). Next, the propagated error of the analytical uncertainty considers the measured concentration uncertainty only, and does not include uncertainties in production rate, the calibrated radiocarbon ages of the moss, and potential isotope production beneath thin ice. Due to the significant contribution of muon-produced ^{14}C in the subsurface, varying degrees of partial ^{14}C production through thin ice (<50 m) can occur. In order for the ^{14}C concentration to decay to our measured values, longer durations of ice cover would be required under thin ice

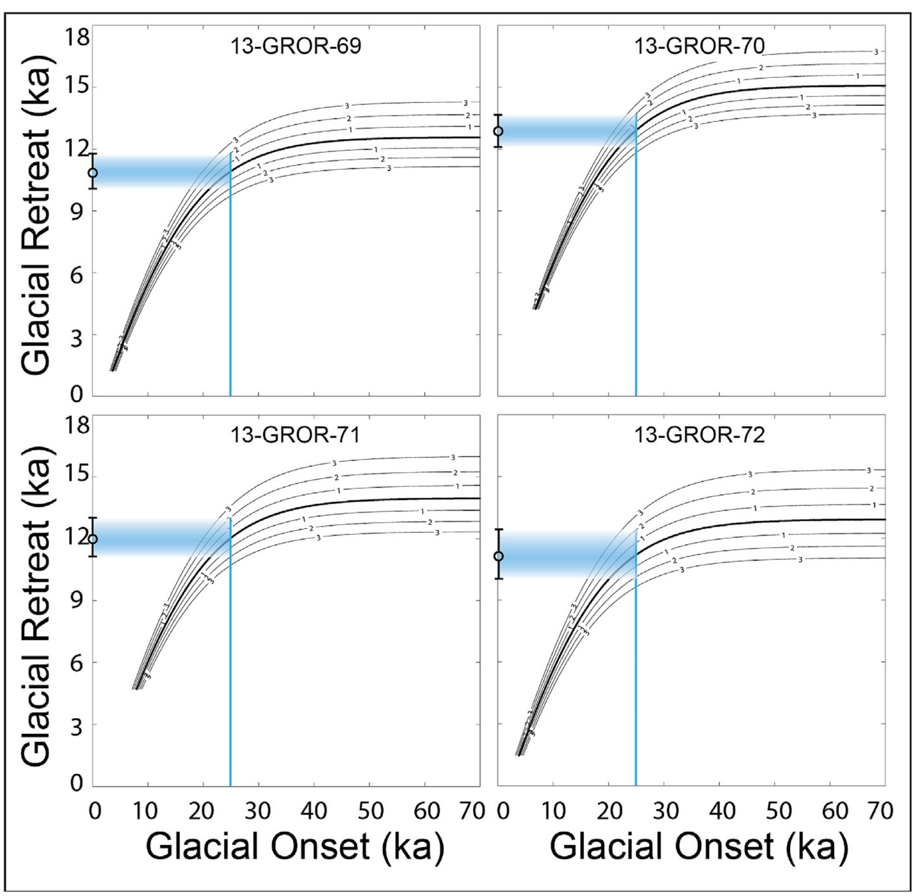

Fig. 5. Plausible glacial onset ages (x axis) versus glacial retreat ages (y axis) for the four sample locations. 1, 2, and 3 sigma uncertainties for the solutions are shown (thin black lines). Each solution curve (thick black line) shows the age of LGM deglaciation required for a particular LGM onset age, and vice versa. The plots also show the insensitivity of ^{14}C to longer periods of exposure as seen for burial beginning ~30 ka, as the curve flattens. The youngest limits of the curve are constrained by the moss radiocarbon ages. Scenario C (see text) is shown with the vertical blue line as the onset of glaciation (25 ka) and the fuzzy blue region/error bars as the 2-sigma measured concentration uncertainty of glacial retreat (the last deglaciation). (For interpretation of the references to color in this figure legend, the reader is referred to the Web version of this article.)

scenarios, thus resulting in younger deglacial ages or an earlier onset of glaciation during the LGM (Fig. 7; Hippe, 2017; Schweinsberg et al., 2018, 2019; Pendleton et al., 2019). Due to the lack of information about ice thickness of Holocene ice caps or earlier ice cover, we opt not to include ice thickness in the models, but show several thin ice possibilities and how thin ice cover would affect surface history (Fig. 7).

3. Results and interpretation

The measured *in situ* ^{14}C concentrations for each sample range from 209,100 ± 7300 at/g to 297,400 ± 6300 at/g (Table 1). These concentrations yield apparent exposure ages between 4.6 and 10.7 ka. Since these are apparent ages and therefore do not account for periods of decay or inheritance, the results from our forward modelling are used in all further discussion.

Our model results provide a solution for possible exposure/burial scenarios (Fig. 5). The solution space is a means of identifying a plausible solution from a given timing of glacial onset, or when ice covered the sample location, and deglaciation, or when ice melts away and exposes the sample location. It also provides the 1, 2, and 3 sigma ranges as contour lines based on the uncertainty of each *in situ* ^{14}C measurement. Because of the non-unique nature of the model, additional *a priori* knowledge is necessary to constrain each sample's exposure/burial history. Such *a priori* knowledge may be derived from independent sources such as reworked bivalves from northern Greenland (England, 1999; Larsen et al., 2018) or lake sediments (Briner et al., 2007). If external evidence provides an age of burial due to glaciation onset, a vertical line and its uncertainties is projected from the x axis onto the graph, and the corresponding age and uncertainty of deglaciation is projected horizontally onto the y axis. Similarly, the solution space can be queried directly to determine the corresponding solutions.

Based on our analysis, we next present end-member scenarios for each sample: (A) continuous exposure throughout the LGM (labeled "nunatak" in Fig. 6A), or (B) complete burial during a sufficiently long LGM (e.g., ≥30 kyr) with thick ice (e.g., ≥50 m) (Hippe, 2017) that leads to the complete decay of *in situ* ^{14}C by the time of deglaciation (Fig. 6B). In addition, we model a third intermediate scenario (scenario C) that simulates a plausible LGM history based on published timing of the LGM onset elsewhere in Greenland at ~25 ka (Fig. 6c) (England, 1999; Larsen et al., 2018). Sample concentrations in scenarios (B) and (C) are made to experience the same Holocene ice cap history, dictated for each sample by their site-specific moss radiocarbon ages. Thus, given the Holocene ice cap cover as a known value, the timing of deglaciation for each site is solved for. Sample concentrations in scenario (A) are solved for only one period of ice cover with radioactive decay from saturation and then compared to the moss radiocarbon ages for the timing of Holocene ice cap burial.

3.1. Scenario A: LGM nunatak

In scenario A, we modelled no ice sheet burial during the LGM (nunatak end member). In this case, we allow each sample to reach a steady state prior to the LGM and remain saturated until burial during Neoglaciation, or the most recent episode of ice cap expansion observed in the Holocene (Schweinsberg et al., 2017, 2018, 2019). We find that the measured concentrations are too low to be explained with the duration of ice cap burial dictated solely by the moss radiocarbon ages. Additional burial ranging from 2500 to 3500 years would be required (Fig. 6A, Table 2). If partial *in situ* ^{14}C production were to occur through ice less than 50 m thick, then the measured concentrations would require even longer periods of Holocene burial, which is a further departure from existing constraints (Fig. 7A; Hippe, 2017; Schweinsberg et al., 2018, 2019; Pendleton et al., 2019).

Table 1
Sample location and measurement results. Moss data from Schweinsberg et al. (2017).

Sample	Lat (°N)	Long (°W)	Elev (m asl)	Thickness (cm)	^{14}C Concentration (at/g)	Production Rate (at/g/yr)	Moss Age (cal yr BP)
13-GROR-69	70.68753	−51.82554	1184	2.5	297400 ± 6300	55.8	1220 ± 40
13-GROR-70	70.90289	−52.05151	1497	2.0	258100 ± 5700	71.1	4220 ± 70
13-GROR-71	71.00298	−51.69919	1404	2.0	209100 ± 7300	66.1	4690 ± 110
13-GROR-72	70.97373	−51.42089	1208	2.0	293800 ± 8300	56.5	1460 ± 60

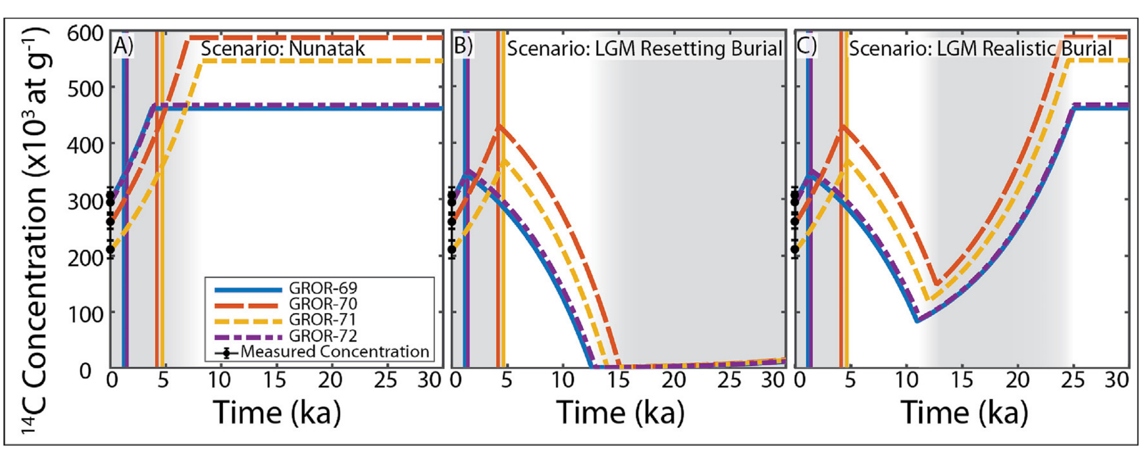

Fig. 6. ^{14}C concentration-through-time plots for two end member scenarios representing continuous LGM exposure (A) and complete nuclide decay (B); an intermediate burial example based on published work is shown in (C). The measured *in situ* ^{14}C concentrations and 2-sigma measurement uncertainty for the four samples are located on the y axis. The vertical lines represent the age of Holocene ice cap growth as determined by the moss radiocarbon ages at each site. Grey regions signify burial by ice cover.

Table 2
Modelled sample history results. The ± values are the asymmetric 2 sigma uncertainties.

Sample	Moss age[a]	Apparent Age		Scenario A		Scenario B		Scenario C	
		in situ ^{14}C		Total Holocene burial required		Modelled deglaciation		Modelled deglaciation	
13-GROR-69	1220	10700	+1000 −900	3740	+370 −350	12280	+1090 −960	10690	+890 −8000
13-GROR-70	4220	5500	+400 −300	7000	+390 −370	14580	+1020 −910	12550	+780 −720
13-GROR-71	4690	4600	+400 −400	8200	+630 −580	13460	+1230 −1080	11650	+980 −870
13-GROR-72	1460	10100	+1200 −1100	3950	+500 −460	12600	+1500 −1280	10950	+1220 −1050

[a] Cal yr BP, median age from Schweinsberg et al. (2017).

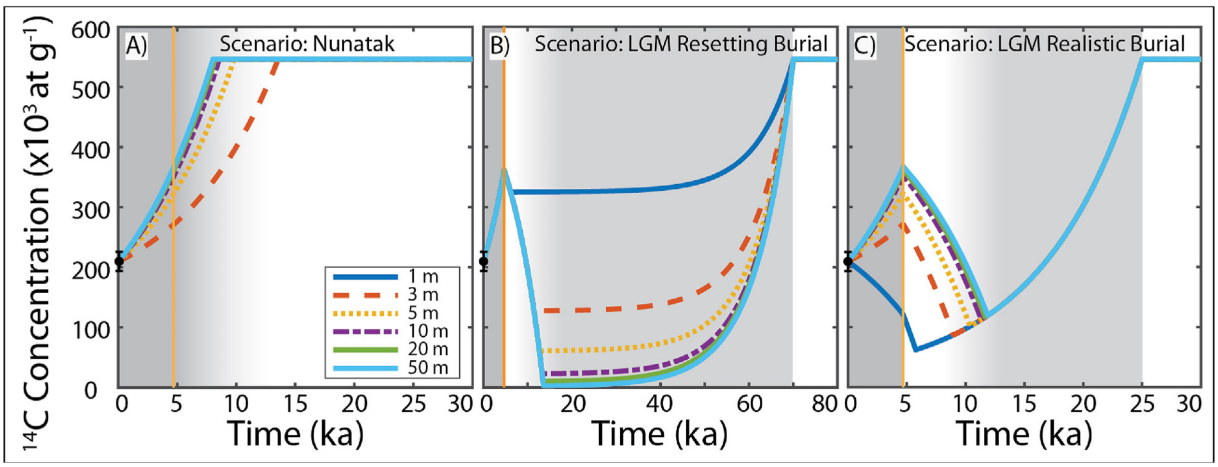

Fig. 7. The effects of different ice thicknesses during burial on the ^{14}C concentration through time. A) represents the Nunatak scenario from Fig. 6A B) represents thin ice only during the LGM, and C) represents thin ice only during the Holocene with burial set to 25 ka with 50 m of ice and the moss age of 4.7 ka. All panels are for sample 13-GROR-71 with varying ice thicknesses of 1 m, 3 m, 5 m, 10 m, 20 m, and 50 m. Note how concentration trajectories nearly overlap for 10–50 m. Panel A) does not show a 1 m equivalent ice thickness because no solution existed for ice less than 2 m thick. As the ice thins, the duration of burial by ice must increase in order to achieve the measured concentration. B) Note the change to a longer x-axis to show the adjustment to equilibrium through the ice. The constant ice thickness represents an integrated ice thickness rather than determining ice thickening and thinning through time.

3.2. Scenario B: LGM burial

For scenario B, we modelled thick LGM ice growth for a sufficiently long time that would allow previously accumulated *in situ* ^{14}C to completely decay away. The minimum duration of burial for this to occur is 25–30 kyr depending on the detection limit. Using existing constraints for Neoglacial ice cap burial (moss ages), *in situ* ^{14}C concentrations can be used to solve for deglaciation ages between 12 and 15 ka at all four sample sites (Table 2). If deglaciation took place earlier, there would be higher nuclide concentrations than we measured, and additional periods of ice-cap burial post-deglaciation would be required. Under the guidelines of this scenario, deglaciation could not occur any later unless insufficiently thick ice cover allowed partial *in situ* ^{14}C accumulation during the LGM (Fig. 7B). If thin ice were present during the late Holocene burial phase, the solutions for LGM deglaciation would be younger (Fig. 7C; Schweinsberg et al., 2018, 2019).

3.3. Scenario C: a plausible ice sheet history

While the above two end members bracket possible interpretations of the *in situ* ^{14}C concentrations, additional LGM burial/exposure scenarios could plausibly explain the results. For a third scenario, we utilized published estimates for the onset of the LGM on Greenland from Larsen et al. (2018) for northeastern Greenland, and from England (1999) for northwestern Greenland. Both datasets provide radiocarbon ages of re-worked marine bivalves, the youngest of which constrain the timing of the LGM onset. Based on these studies, scenario C was generated with the GrIS advancing over the sample locations at ~25 ka. With this constraint for the onset of LGM burial and using the moss ages as constraints for the duration of Neoglacial burial, our modelled histories result in deglaciation ages ranging from 10.7 to 12.5 ka, with each containing *in situ* ^{14}C inheritance in the bedrock surfaces upon deglaciation.

4. Discussion

For our sample locations to have been LGM nunataks, additional Holocene burial would be required. The moss ages only record the most recent interval of burial under an ice cap, and it is therefore plausible that an earlier period of ice cap burial existed followed by a brief ice-free period, as revealed for some sites in southwestern Greenland by Schweinsberg et al. (2018). Therefore, the modelled additional burial of 2490–3510 years could have occurred during an earlier period of ice cap cover, such as at other times during the Holocene or perhaps during the Younger Dryas. Due to the moss only recording the most recent period of ice expansion over a sample location, the timing of earlier periods of ice expansion remain unknown.

The majority of the data presented in Schweinsberg et al. (2018) show that moss radiocarbon ages record the entire duration of Holocene ice cover. In addition, the oldest radiocarbon age of ice-killed moss on Greenland is ~5 ka, yet sample 13GROR-71 would require at least 8200 years of burial to be compatible with that site being an LGM nunatak. Furthermore, several proglacial lake sediment records show no significant ice cap expansion until ~4 ka (Balascio et al., 2015; Schweinsberg et al., 2017, 2019). Thus, in the context of the climate history and moss chronology of the region, the likelihood that these four sample locations were nunataks during the LGM is possible, but may not be the most plausible explanation based on the measured *in situ* ^{14}C inventories.

The long duration of thick LGM ice cover required in scenario B is not plausible given the context of the overall ^{10}Be/^{26}Al concordant concentrations. Evidence from NW and NE Greenland indicates that the GrIS was roughly the same size as the current ice sheet during MIS 3 (57−28 ka) and may not have advanced beyond the present ice sheet footprint until after ~25 ka (England, 1999; Larsen et al., 2018).

In scenario C, the age of initial ice cover at ca. 25 ka is used to yield deglaciation ages at our sample sites ranging from 10.7 to 12.6 ka. This age range lies between the deglaciation age from the continental shelf break at ~15 ka (O'Cofaigh et al., 2013; Sheldon et al., 2016) and the deglaciation age near the present ice margin in central Uummannaq at ~10.8 ka (Philipps et al., 2018). We argue that following recession of the ice terminus from the LGM limit, the inner ice streams would begin to thin, isolating the high elevation locations from the main ice sheet. In this scenario, the ice cover would eventually melt away to expose the bedrock underneath, resuming the build-up of *in situ* ^{14}C in addition to the inherited nuclide inventories already present in the rock surfaces. The main ice sheet would then retreat inland past the present-day margin at ~10.8 ka and, with an overall cooling climate ~5 ka, the local ice caps would develop during Neoglaciation (Philipps et al., 2018; Schweinsberg et al., 2017, 2018, 2019).

A known constraint based on the ^{10}Be/^{26}Al ratios in our samples is that the maximum cumulative period of ice cover cannot exceed ~87−189 kyr (Beel et al., 2016). This maximum limiting duration of burial therefore provides a useful *a priori* constraint. With a late onset of LGM ice (Scenario C), the total duration of burial during Neoglaciation and the LGM combined is 15.5−18.0 kyr; this value is within the maximum amount of allowable burial even if this duration of burial was repeated over the past several glacial-interglacial cycles (Strunk et al., 2017). However, if we instead used the benthic δ^{18}O stack from Lisiecki and Raymo (2005) as a guide for the exposure/burial history of our sample sites, combined with the observation that our sites are partially glaciated by local ice at present (even during an interglacial), then our sites would be ice-free for much less time than they are ice-covered; that is, with the glacial/interglacial threshold set to allow for ice cover during present conditions (Knudsen et al., 2015; Knudsen and Egholm, 2018). In this case, there would be too much burial and not enough exposure to be consistent with the long durations of exposure with insignificant burial as indicated by the ^{26}Al/^{10}Be data.

We interpret our study sites as being partially glaciated during interglacial conditions (Late Holocene) and during the peak of a glacial period but exposed between these intervals. If these sites were nunataks during the LGM, then they would only be covered during minima in the δ^{18}O stack (Fig. 4; Strunk et al., 2017). It is also important to note that the δ^{18}O stack is a proxy of a combination of ocean temperature and global ice volume, not just ice volume. Thus, while this may (or may not) be an appropriate proxy for the size of any single ice sheet such as the GrIS, it is likely decoupled from forcings that affect small ice caps. Following scenario C, if our sites were ice-free during MIS 3 and the early Holocene, but covered by ice during the LGM (MIS 2) and the late Holocene, then the source and availability of precipitation in the region likely played a key role in the development of coastal ice caps (Bintanja and Selten, 2014; England, 1999; Ledu et al., 2010; Thomas et al., 2018). For example, if Baffin Bay was covered by perennial sea ice during times of maximum ice sheet extent, the lack of locally sourced precipitation could have prevented sustained local ice cap growth in the coastal uplands of western Greenland. Similarly, the presence of thick, multiyear sea ice or shelf ice in Baffin Bay may have also affected the GrIS locally as well as influenced ocean circulation-atmosphere interactions. This could allow the uplands to become covered by the GrIS, and at the same time, serve to keep precipitation too low for fueling local ice cap cover immediately before and after maximum GrIS conditions.

5. Conclusion

Results from this study shed light on the ice cover history of coastal uplands in central West Greenland. The forward modelling of our *in situ* ^{14}C measurements suggests that additional Holocene ice cover in excess of that observed in the regional moss and proglacial lake paleoenvironmental chronologies (Schweinsberg et al., 2018) is needed for the uplands to have persisted as nunataks during the LGM. While the lack of glacial erosion and ^{10}Be/^{26}Al data provides some support for the hypothesis that these locations were LGM nunataks, the addition of *in situ* ^{14}C measurements supports the possibility of ice cover during the LGM, consistent with the findings of Strunk et al. (2017). Whether this ice cover was by local ice or the GrIS remains unclear. Regardless, this study provides an important constraint for the development of ice sheet models through the onset and duration of ice cover in the central Uummannaq uplands.

While only one scenario (scenario C) was directly identified as having a plausible ice cover history, the results from this analysis can be coupled with more sophisticated ice sheet models to tune the lateral extent and thickness of ice. Additionally, if these locations were intermittently covered by local ice rather than by the GrIS during the past few glacial/interglacial cycles, then ice cover models using a threshold value on the benthic δ^{18}O stack may not accurately represent the true ice cover history. A more sophisticated model utilizing climate and precipitation may be necessary. For the Uummannaq region, the influence of sea ice in Baffin Bay on the availability of precipitation may be an important factor in determining ice cap dynamics.

Declarations

All authors contributed to the manuscript.

Author contribution

BLG: Formal Analysis, Methodology, Software, Validation, Visualization, Writing-Original Draft.

JPB: Conceptualization, Data and sample acquisition, Methodology, Project Administration, Validation, Writing − Original Draft/review and editing.

ADS: Data and sample acquisition, Writing-Review and editing, Investigation, Conceptualization.

NAL: Sample processing, Resources, Review and editing.

OB: Resources, Funding Acquisition.

Declaration of competing interest

None.

Acknowledgements

We would like to thank CH2M Hill Polar Field services for logistical support and the United States 109th Air Lift Wing Air National Guard. We thank Casey Beel, Alia Lesnek, and Christopher Sbarra for assistance in the laboratory. This manuscript was improved by the efforts of two anonymous reviewers. This research was supported by National Science Foundation grant ARC-1204005.

Appendix A. Supplementary data

Supplementary data to this article can be found online at https://doi.org/10.1016/j.quascirev.2019.105981.

References

Anderson, R.K., Miller, G.H., Briner, J.P., Lifton, N.A., DeVogel, S.B., 2008. A millennial perspective on Arctic warming from ^{14}C in quartz and plants emerging from beneath ice caps. Geophys. Res. Lett. 35 https://doi.org/10.1029/2007GL032057.

Arndt, J.E., Jokat, W., Dorschel, B., 2017. The last glaciation and deglaciation of the Northeast Greenland continental shelf revealed by hydro-acoustic data. Quat. Sci. Rev. 160, 45–56. https://doi.org/10.1016/j.quascirev.2017.01.018.

Balascio, N.L., D'Andrea, W.J., Bradley, R.S., 2015. Glacier response to north Atlantic climate variability during the Holocene. Clim. Past 11, 1587–1598. https://doi.org/10.5194/cp-11-1587-2015.

Balco, G., 2017. Production rate calculations for cosmic-ray-muon-produced 10 Be and 26 Al benchmarked against geological calibration data. Quat. Geochronol. 39, 150–173. https://doi.org/10.1016/j.quageo.2017.02.001.

Beel, C.R., Lifton, N.A., Briner, J.P., Goehring, B.M., 2016. Quaternary evolution and ice sheet history of contrasting landscapes in Uummannaq and Sukkertoppen, western Greenland. Quat. Sci. Rev. 149, 248–258. https://doi.org/10.1016/j.quascirev.2016.05.033.

Bierman, P.R., Marsella, K.A., Patterson, C., Davis, P.T., Caffee, M., 1999. Mid-Pleistocene cosmogenic minimum-age limits for pre-Wisconsinan glacial surfaces in southwestern Minnesota and southern Baffin Island: a multiple nuclide approach. Geomorphology 27, 25–39. https://doi.org/10.1016/S0169-555X(98)00088-9.

Bintanja, R., Selten, F.M., 2014. Future increases in Arctic precipitation linked to local evaporation and sea-ice retreat. Nature 509, 479–482. https://doi.org/10.1038/nature13259.

Borchers, B., Marrero, S., Balco, G., Caffee, M., Goehring, B., Lifton, N., Nishiizumi, K., Phillips, F., Schaefer, J., Stone, J., 2016. Geological calibration of spallation production rates in the CRONUS-Earth project. Quat. Geochronol. 31, 188–198. https://doi.org/10.1016/j.quageo.2015.01.009.

Briner, J.P., Axford, Y., Forman, S.L., Miller, G.H., Wolfe, A.P., 2007. Multiple generations of interglacial lake sediment preserved beneath the Laurentide Ice Sheet. Geology 35, 887–890. https://doi.org/10.1130/G23812A.1.

Briner, J.P., Lifton, N.A., Miller, G.H., Refsnider, K., Anderson, R., Finkel, R., 2014. Using in situ cosmogenic 10Be, 14C, and 26Al to decipher the history of polythermal ice sheets on Baffin Island, Arctic Canada. Quat. Geochronol. 19, 4–13. https://doi.org/10.1016/j.quageo.2012.11.005.

Briner, J.P., McKay, N.P., Axford, Y., Bennike, O., Bradley, R.S., de Vernal, A., Fisher, D., Francus, P., Fréchette, B., Gajewski, K., Jennings, A., Kaufman, D.S., Miller, G., Rouston, C., Wagner, B., 2016. Holocene climate change in Arctic Canada and Greenland. Quat. Sci. Rev. 147, 340–364. https://doi.org/10.1016/j.quascirev.2016.02.010.

Briner, J.P., Miller, G.H., Davis, P.T., Bierman, P.R., Caffee, M., 2003. Last Glacial Maximum ice sheet dynamics in Arctic Canada inferred from young erratics perched on ancient tors. Quat. Sci. Rev. 22, 437–444. https://doi.org/10.1016/S0277-3791(03)00003-9.

Briner, J.P., Miller, G.H., Davis, P.T., Finkel, R.C., 2006. Cosmogenic radionuclides from fiord landscapes support differential erosion by overriding ice sheets. Geol. Soc. Am. Bull. 118, 406–420. https://doi.org/10.1130/B25716.1.

Corbett, L.B., Bierman, P.R., Graly, J.A., Neumann, T.A., Rood, D.H., 2013. Constraining landscape history and glacial erosivity using paired cosmogenic nuclides in Upernavik, northwest Greenland. GSA Bull. 125, 1539–1553. https://doi.org/10.1130/B30813.1.

Corbett, L.B., Bierman, P.R., Rood, D.H., Caffee, M.W., Lifton, N.A., Woodruff, T.E., 2017. Cosmogenic ^{26}Al/^{10}Be surface production ratio in Greenland: cosmogenic ^{26}Al/^{10}Be production ratio. Geophys. Res. Lett. 44, 1350–1359. https://doi.org/10.1002/2016GL071276.

England, J., 1999. Coalescent Greenland and innuitian ice during the last glacial maximum: revising the quaternary of the Canadian high Arctic. Quat. Sci. Rev. 18, 421–456. https://doi.org/10.1016/S0277-3791(98)00070-5.

Funder, S., Kjeldsen, K.K., Kjær, K.H., Ó Cofaigh, C., 2011. The Greenland ice sheet during the past 300,000 Years: a review. In: Developments in Quaternary Sciences. Elsevier, pp. 699–713.

Gjermundsen, E.F., Briner, J.P., Akçar, N., Foros, J., Kubik, P.W., Salvigsen, O., Hormes, A., 2015. Minimal erosion of Arctic alpine topography during late Quaternary glaciation. Nat. Geosci. 8, 789–792. https://doi.org/10.1038/ngeo2524.

Hall, A.M., Phillips, W.M., 2006. Glacial modification of granite tors in the Cairngorms, Scotland. J. Quat. Sci. 21, 811–830. https://doi.org/10.1002/jqs.1003.

Hippe, K., 2017. Constraining processes of landscape change with combined in situ cosmogenic 14 C- 10 Be analysis. Quat. Sci. Rev. 173, 1–19. https://doi.org/10.1016/j.quascirev.2017.07.020.

Hippe, K., Lifton, N.A., 2014. Calculating isotope ratios and nuclide concentrations for in situ cosmogenic 14C analyses. Radiocarbon 56, 1167–1174. https://doi.org/10.2458/56.17917.

Kelly, M., 1985. A review of the Quaternary geology of western Greenland. In: Andrews, J.T. (Ed.), Quaternary Environments in Eastern Canadian Arctic, Baffin Bay and Western Greenland. Allen and Unwin, Boston, pp. 461–501.

Knudsen, M.F., Egholm, D.L., 2018. Constraining Quaternary ice covers and erosion rates using cosmogenic 26 Al/10 Be nuclide concentrations. Quat. Sci. Rev. 181, 65–75. https://doi.org/10.1016/j.quascirev.2017.12.012.

Knudsen, M.F., Egholm, D.L., Jacobsen, B.H., Larsen, N.K., Jansen, J.D., Andersen, J.L., Linge, H.C., 2015. A multi-nuclide approach to constrain landscape evolution and past erosion rates in previously glaciated terrains. Quat. Geochronol. 30, 100–113. https://doi.org/10.1016/j.quageo.2015.08.004.

Lane, T.P., Roberts, D.H., Rea, B.R., Ó Cofaigh, C., Vieli, A., Rodés, A., 2014. Controls upon the last glacial maximum deglaciation of the northern Uummannaq ice stream system, west Greenland. Quat. Sci. Rev. APEX II Arctic Palaeoclim. Extrem. 92, 324–344. https://doi.org/10.1016/j.quascirev.2013.09.013.

Larsen, N.K., Levy, L.B., Carlson, A.E., Buizert, C., Olsen, J., Strunk, A., Bjørk, A.A., Skov, D.S., 2018. Instability of the Northeast Greenland ice stream over the last 45,000 years. Nat. Commun. 9 https://doi.org/10.1038/s41467-018-04312-7.

Lecavalier, B.S., Milne, G.A., Simpson, M.J.R., Wake, L., Huybrechts, P., Tarasov, L., Kjeldsen, K.K., Funder, S., Long, A.J., Woodroffe, S., Dyke, A.S., Larsen, N.K., 2014. A model of Greenland ice sheet deglaciation constrained by observations of relative sea level and ice extent. Quat. Sci. Rev. 102, 54–84. https://doi.org/10.1016/j.quascirev.2014.07.018.

Ledu, D., Rochon, A., de Vernal, A., Barletta, F., St-Onge, G., 2010. Holocene sea ice history and climate variability along the main axis of the Northwest Passage, Canadian Arctic: holocene IN the northwest passage. Paleoceanography 25. https://doi.org/10.1029/2009PA001817.

Lifton, N., Caffee, M., Finkel, R., Marrero, S., Nishiizumi, K., Phillips, F.M., Goehring, B., Gosse, J., Stone, J., Schaefer, J., Theriault, B., Jull, A.J.T., Fifield, K., 2015. In situ cosmogenic nuclide production rate calibration for the CRONUS-Earth project from Lake Bonneville, Utah, shoreline features. Quat. Geochronol. CRONUS-EARTH Vol. Part I 26, 56–69. https://doi.org/10.1016/j.quageo.2014.11.002.

Lifton, N., Sato, T., Dunai, T.J., 2014. Scaling in situ cosmogenic nuclide production rates using analytical approximations to atmospheric cosmic-ray fluxes. Earth Planet. Sci. Lett. 386, 149–160. https://doi.org/10.1016/j.epsl.2013.10.052.

Lisiecki, L.E., Raymo, M.E., 2005. A Pliocene-Pleistocene stack of 57 globally distributed benthic δ^{18}O records: pliocene-pleistocene benthic stack. Paleoceanography 20. https://doi.org/10.1029/2004PA001071 n/a-n/a.

McKay, N.P., Kaufman, D.S., Routson, C.C., Erb, M.P., Zander, P.D., 2018. The onset and rate of Holocene neoglacial cooling in the Arctic. Geophys. Res. Lett. 45 (12) https://doi.org/10.1029/2018GL079773, 487-12,496.

Miller, G., Briner, J., Lifton, N., Finkel, R., 2006. Limited ice-sheet erosion and complex exposure histories derived from in situ cosmogenic 10Be, 26Al, and 14C on Baffin Island, Arctic Canada. Quat. Geochronol. 1, 74–85. https://doi.org/10.1016/j.quageo.2006.06.011.

Miller, G.H., Lehman, S.J., Refsnider, K.A., Southon, J.R., Zhong, Y., 2013. Unprecedented recent summer warmth in Arctic Canada: unprecedented arctic warmth. Geophys. Res. Lett. 40, 5745–5751. https://doi.org/10.1002/2013GL057188.

Morlighem, M., Williams, C.N., Rignot, E., An, L., Arndt, J.E., Bamber, J.L., Catania, G., Chauché, N., Dowdeswell, J.A., Dorschel, B., Fenty, I., Hogan, K., Howat, I., Hubbard, A., Jakobsson, M., Jordan, T.M., Kjeldsen, K.K., Millan, R., Mayer, L., Mouginot, J., Noël, B.P.Y., O'Cofaigh, C., Palmer, S., Rysgaard, S., Seroussi, H., Siegert, M.J., Slabon, P., Straneo, F., van den Broeke, M.R., Weinrebe, W., Wood, M., Zinglersen, K.B., 2017. BedMachine v3: complete bed topography and ocean Bathymetry mapping of Greenland from multibeam echo sounding combined with mass conservation. Geophys. Res. Lett. 44, 11051–11061. https://doi.org/10.1002/2017GL074954.

O'Cofaigh, C., Dowdeswell, J.A., Jennings, A.E., Hogan, K.A., Kilfeather, A., Hiemstra, J.F., Noormets, R., Evans, J., McCarthy, D.J., Andrews, J.T., Lloyd, J.M., Moros, M., 2013. An extensive and dynamic ice sheet on the West Greenland shelf during the last glacial cycle. Geology 41, 219–222. https://doi.org/10.1130/G33759.1.

Pendleton, S.L., Miller, G.H., Lifton, N., Lehman, S.J., Southon, J., Crump, S.E., Anderson, R.S., 2019. Rapidly receding Arctic Canada glaciers revealing landscapes continuously ice-covered for more than 40,000 years. Nat. Commun. 10, 445. https://doi.org/10.1038/s41467-019-08307-w.

Philipps, W., Briner, J.P., Bennike, O., Schweinsberg, A., Beel, C., Lifton, N., 2018. Earliest Holocene deglaciation of the central Uummannaq Fjord system, West Greenland. Boreas 47, 311–325. https://doi.org/10.1111/bor.12270.

Phillips, F.M., Argento, D.C., Balco, G., Caffee, M.W., Clem, J., Dunai, T.J., Finkel, R., Goehring, B., Gosse, J.C., Hudson, A.M., Jull, A.J.T., Kelly, M.A., Kurz, M., Lal, D., Lifton, N., Marrero, S.M., Nishiizumi, K., Reedy, R.C., Schaefer, J., Stone, J.O.H., Swanson, T., Zreda, M.G., 2016. The CRONUS-Earth Project: a synthesis. Quat. Geochronol. 31, 119–154. https://doi.org/10.1016/j.quageo.2015.09.006.

Rinterknecht, Vincent, Gorokhovich, Yuri, Schaefer, Joerg, Caffee, Marc, 2009. Preliminary 10Be chronology for the last deglaciation of the western margin of the

Greenland Ice Sheet. J. Quat. Sci. 24, 270–278. https://doi.org/10.1002/jqs.1226.

Roberts, D.H., Long, A.J., Schnabel, C., Davies, B.J., Xu, S., Simpson, M.J.R., Huybrechts, P., 2009. Ice sheet extent and early deglacial history of the southwestern sector of the Greenland Ice Sheet. Quat. Sci. Rev. 28, 2760–2773. https://doi.org/10.1016/j.quascirev.2009.07.002.

Roberts, D.H., Rea, B.R., Lane, T.P., Schnabel, C., Rodés, A., 2013. New constraints on Greenland ice sheet dynamics during the last glacial cycle: evidence from the Uummannaq ice stream system. J. Geophys. Res. Earth Surf. 118, 519–541. https://doi.org/10.1002/jgrf.20032.

Schweinsberg, A.D., Briner, J.P., Licciardi, J.M., Bennike, O., Lifton, N.A., Graham, B.L., Young, N.E., Schaefer, J.M., Zimmerman, S.H., 2019. Multiple independent records of local glacier variability on Nuussuaq, West Greenland, during the Holocene. Quat. Sci. Rev. 215, 253–271. https://doi.org/10.1016/j.quascirev.2019.05.007.

Schweinsberg, A.D., Briner, J.P., Miller, G.H., Bennike, O., Thomas, E.K., 2017. Local glaciation in west Greenland linked to north Atlantic ocean circulation during the Holocene. Geology 45, 195–198. https://doi.org/10.1130/G38114.1.

Schweinsberg, A.D., Briner, J.P., Miller, G.H., Lifton, N.A., Bennike, O., Graham, B.L., 2018. Holocene mountain glacier history in the Sukkertoppen Iskappe area, southwest Greenland. Quat. Sci. Rev. 197, 142–161. https://doi.org/10.1016/j.quascirev.2018.06.014.

Sheldon, C., Jennings, A., Andrews, J.T., Ó Cofaigh, C., Hogan, K., Dowdeswell, J.A., Seidenkrantz, M.-S., 2016. Ice stream retreat following the LGM and onset of the west Greenland current in Uummannaq Trough, west Greenland. Quat. Sci. Rev. Spec. Issue PAST Gateways (Palaeo-Arctic Spat. Temporal Gateways) 147, 27–46. https://doi.org/10.1016/j.quascirev.2016.01.019.

Strunk, A., Knudsen, M.F., Egholm, D.L., Jansen, J.D., Levy, L.B., Jacobsen, B.H., Larsen, N.K., 2017. One million years of glaciation and denudation history in west Greenland. Nat. Commun. 8, 14199. https://doi.org/10.1038/ncomms14199.

Thomas, E.K., Castañeda, I.S., McKay, N.P., Briner, J.P., Salacup, J.M., Nguyen, K.Q., Schweinsberg, A.D., 2018. A wetter Arctic coincident with hemispheric warming 8,000 Years ago. Geophys. Res. Lett. 45, 10637–10647. https://doi.org/10.1029/2018GL079517.

Vasskog, K., Langebroek, P.M., Andrews, J.T., Nilsen, J.E.Ø., Nesje, A., 2015. The Greenland Ice Sheet during the last glacial cycle: current ice loss and contribution to sea-level rise from a palaeoclimatic perspective. Earth Sci. Rev. 150, 45–67. https://doi.org/10.1016/j.earscirev.2015.07.006.

Walker, M., Head, M.J., Berkelhammer, M., Björck, S., Cheng, H., Cwynar, L., Fisher, D., Gkinis, V., Long, A., Lowe, J., Newnham, R., Rasmussen, S.O., Weiss, H., 2018. Formal ratification of the subdivision of the Holocene series/epoch (quaternary system/period): two new global boundary stratotype sections and points (GSSPs) and three new stages/subseries. Episodes 41, 213–223. https://doi.org/10.18814/epiiugs/2018/018016.

Young, N.E., Lamp, J., Koffman, T., Briner, J.P., Schaefer, J., Gjermundsen, E.F., Linge, H., Zimmerman, S., Guilderson, T.P., Fabel, D., Hormes, A., 2018. Deglaciation of coastal south-western Spitsbergen dated with in situ cosmogenic 10Be and 14C measurements. J. Quat. Sci. 33, 763–776. https://doi.org/10.1002/jqs.3058.